

This is the author-manuscript version of this work - accessed from <http://eprints.qut.edu.au>

Frost, Ray L. and Daniel, Lisa M. and Zhu, Huaiyong (2007) Synthesis and characterisation of clay-supported titania photocatalysts. *Journal of Colloid and Interface Science* 316(1):pp. 72-79.

Copyright 2007 Elsevier

Synthesis and characterisation of clay-supported titania photocatalysts

Lisa M. Daniel, Ray L. Frost^{*}, Huai Yong Zhu

Inorganic Materials Research Program, School of Physical and Chemical Sciences, Queensland University of Technology, GPO Box 2434, Brisbane Queensland 4001, Australia. Email: r.frost@qut.edu.au

Abstract

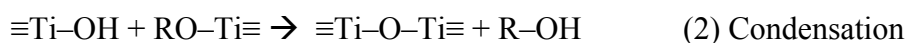
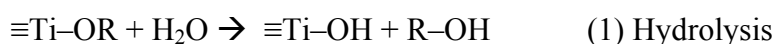
This study examines the use of laponite, a synthetic smectite, which forms exfoliated silicate layers when dispersed in water, as an inorganic support for titania nanocrystals. Titania nanocrystals are prepared prior to addition to the clay dispersion, by a sol-gel synthesis incorporating a microwave hydrothermal step. The characteristics of the resultant structure such as titania phase, crystallite size and particulate size are examined via X-Ray Diffraction (XRD), Transmission Electron Spectroscopy (TEM) and Infrared Spectroscopy.

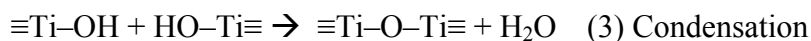
Key words: titania; photocatalyst; laponite; colloid, surfactant, hydrothermal treatment .

1. Introduction

Titanium dioxide (TiO₂) has been extensively investigated as a photocatalyst for environmental remediation, as it is photostable, non-toxic, highly reactive and is a relatively inexpensive material [1-5]. When TiO₂ is illuminated by UV light ($\lambda \leq 387\text{nm}$), a photo-generated hole (h⁺) and electron (e⁻) pair may be produced. Surface hydroxyl groups are oxidised by the photo-generated holes to produce hydroxyl radicals ($\bullet\text{OH}$) which attack organic species resulting in their degradation into water, carbon dioxide and mineral ions [2, 5]. As this reaction occurs on the TiO₂ particle surface, photocatalytic efficiency is largely dependant on the surface area. Nanosized titania particles have therefore received much interest in this role, possessing enhanced optical, electrical, chemical and catalytic properties.

The most attractive process for the synthesis of TiO₂ nanoparticles is the sol-gel method [7-19]. This process involves the hydrolysis and polycondensation of a metal alkoxide Ti(OR)₄ (R=alkyl groups) precursor and subsequent formation of a gel, which after heat treatment results in a three dimensional crystalline network of linked TiO₆ octahedra [20-22]. The reaction steps may be described by the following equations [23, 24]:





Advantages of the sol-gel method include the ability to control the microstructure [25] and homogeneity [26] of the nanoparticles by varying the alkoxide precursor, the solvent, the addition of acidic or basic additives, and both the synthesis and calcination temperatures [27].

During the treatment of aqueous systems, fine titania particles experience an overwhelming tendency to agglomerate, reducing surface area and ultimately their photocatalytic efficiency. Significant research has focussed on methods of stabilising nano-sized TiO_2 particles on different supports to prevent agglomeration. TiO_2 particles have been immobilised on silica nanospheres [28] and thin films [26, 29-31], on Fe-filled carbon nanocapsules [32], within the interlayer spaces of pillared clays [4, 33] and on the surface of exfoliated clay sheets, such as laponite .

Laponite is a synthetic hectorite, which forms exfoliated silicate layers when dispersed in water [34]. It has a relatively small particle size, with a basic unit consisting of a layered hydrous magnesium silicate platelet of diameter 25-30 nm with a thickness of approximately 1 nm [35]. When laponite powder is dispersed in water, a strongly negative charge appears on the faces of the silicate sheets and a weak positive charge appears on the rim. As a result of these charges, Laponite exhibits face-edge aggregation which leads to relatively open, macroporous structures of aggregates, described as house-of-cards structures. As the pH of the laponite solution

increases, the rim charge decreases, reducing the tendency for aggregation. Tawari et al. suggest that at a pH of 11.7 the rim charge is neutralised .

At high pH values, TiO₂ tends to agglomerate, therefore to ensure the two systems are compatible, surfactants may be employed. Polyethylene oxide (PEO), when added to a clay dispersion of low pH, is found to inhibit aggregation by steric hindrance. The surfactant wraps around the clay particle preventing the positive rims and negative faces of the clay particles from interacting [36]. TiO₂ may then be immobilised on the clay surface and the PEO removed via calcination.

The aim of this paper is to describe the synthesis of laponite clay-supported titania nanoparticles and to examine the effect of synthesis conditions on the physical structure of the materials, using x-ray diffraction, transmission electron microscopy and infrared spectroscopy. Photocatalytic tests of the materials will also be performed to assess their activity.

2. Experimental

2.1. Synthesis of titania nanoparticles

TiO₂ colloids were prepared by the hydrolysis of titanium tetraisopropoxide (TPT) in deionised water according to an experimental procedure described by Wilston et al [37]. Titanium tetraisopropoxide (62.5cm³) and isopropanol (10.0cm³) were combined in a drop funnel and added over a 10 minute period, with vigorous

stirring, to ultrapure deionised water (375cm^3) in a flat-based conical flask. Upon completion of the addition, 69% nitric acid (2.65cm^3) was added to the flask, and the resultant solution refluxed at 80°C with continuous stirring for 18 hours. For comparison, a sample of TiO_2 was prepared using 0.1M nitric acid as a peptising agent.

The resultant colloidal solutions were obtained and transferred to a Teflon-lined polycarbonate vessel for microwave hydrothermal treatment. A MicroSynth Labstation microwave ($1200 \pm 50\text{W}$, 2.45GHz, Milestone MLS) was used at a setting of 80% power, with a pressure ramp from ambient to 60psi over a 10 minute period, with a corresponding temperature of 145°C . Temperature in the reaction vessel was automated by the ATC-FO fiber optic probe, and pressure was maintained by the APC-55E pressure control. The TiO_2 colloid was treated at this temperature and pressure for a 15 minute period, to yield a white suspension. For comparison, hydrothermal treatment of the TiO_2 colloid was also performed in an oven at 180°C for 24 hours to yield a thick white suspension.

2.2. Dispersion of laponite

Laponite clay (Laponite RD) was obtained from Fernz Specialty Chemicals, Australia and used as received. The clay powder has the chemical formula, $\text{Na}_{0.67}\text{K}_{0.01}(\text{Si}_{7.95}\text{Al}_{0.05})-(\text{Mg}_{5.48}\text{Li}_{0.38}\text{Ti}_{0.01})\text{O}_{20}(\text{OH}_4)$, a BET specific surface area of $336.7\text{m}^2/\text{g}$ and a cation exchange capacity of 55 meq per 100 g of clay.

Laponite clay (2g) was added over a period of 5 minutes to ultrapure deionised water (100cm³) with continuous stirring. The suspension was stirred for approximately 30 minutes until it became transparent.

A non-ionic poly(ethylene oxide) surfactant, Tergitol 15S-5, with a general chemical formula of C₁₂₋₁₄H₂₅₋₂₉O(CH₂CH₂O)₅H and an average molecular weight of 420 g/mol was added to some clay dispersions resulting in an opaque solution and stirring was continued for a further 30 minutes. The molar ratio of PEO to Laponite (moles PEO to moles Laponite) employed was 2:1.

2.3. Preparation of TiO₂-clay photocatalysts

To the clay dispersions prepared without surfactant, TiO₂ sol (20mmol Ti/g clay) was added and the pH adjusted to values of 2, 3, 4, 5, 6 and 9 with 0.1M HCl or 0.1M NH₃. The dispersions were stirred for 3 hours, centrifuged, washed with water and dried in an oven at 80°C. The pH parameter is highlighted in the sample names. For example, Ti-L-pH2 is the sample prepared with a pH of 2.

To the clay dispersions prepared with surfactant, TiO₂ sol was added with Ti:clay ratios of 10, 20, 30 and 40mmol of Ti/g of clay. All samples were stirred for 3 hours, hydrothermally treated at 180°C for a period of 24 hours, upon which they were centrifuged, washed with deionised water and dried in an oven at 80°C. They were then calcined at 500°C for a period of 24 hours.

For comparison, samples prepared with 40mmol Ti/g were hydrothermally treated at temperatures of 180, 140 and 80°C and also without any hydrothermal treatment. The two most important parameters: hydrothermal temperature and Ti/Clay ratio were highlighted in the sample names. The number after the letters “Ti-L” indicates the Ti/Clay ratio in mmol of Ti per gram of clay (mmol/g), which are 10, 20, 30 and 40 respectively. The number at the end indicates the hydrothermal temperature. For instance, Ti-L10-180 is the sample prepared with a Ti/Clay ratio of 10 mmol/g and a hydrothermal temperature of 180 °C.

2.4. X-ray diffraction

XRD analyses were performed on a Philips PANalytical X’Pert PRO X-ray diffractometer (radius: 240.0 mm). Incident X-ray radiation was produced from a line focused PW3373/10 Cu X-ray tube, operating at 40 kV and 40 mA, providing a $K\alpha_1$ wavelength of 1.54 Å. The incident beam was monochromated through a 0.020 mm Ni filter then passed through a 0.04 rad. Soller slit, a 15 mm fixed mask and a $\frac{1}{2}^\circ$ fixed anti scatter slit. After interaction with the sample, the diffracted beam passed through a secondary 0.04 rad. Soller slit and a 0.25° progressive divergence slit before detection by an X’Celerator RTMS detector. The detector was set in scanning mode, with an active length of 2.022 mm. Samples were analysed utilising Bragg-Brentano geometry over a range of $1.5 - 70^\circ 2\theta$ with a step size of $0.02^\circ 2\theta$, with each step measured for 12.1 seconds. For all XRD analyses, the samples were dispersed in hexane and dropped onto low background quartz plates, forming a thin film upon evaporation of the hexane.

2.5. Mid-IR spectroscopy

Infrared spectra were obtained using a Nicolet Nexus 870 FTIR spectrometer with a smart endurance single bounce diamond ATR cell. Spectra over the 4000–525 cm^{-1} range were obtained by the co-addition of 64 scans with a resolution of 4 cm^{-1} and a mirror velocity of 0.6329 cm/s . Spectra were co-added to improve the signal to noise ratio.

Spectral manipulation including baseline adjustment, smoothing and normalisation were performed using the Spectralcalc software package GRAMS (Galactic Industries Corporation, NH, USA). Band component analysis was undertaken using the Jandel ‘Peakfit’ software package which enabled the type of fitting function to be selected and allows specific parameters to be fixed or varied accordingly. Band fitting was done using a Lorentz-Gauss cross-product function with the minimum number of component bands used for the fitting process. The Gauss-Lorentz ratio was maintained at values greater than 0.7 and fitting was undertaken until reproducible results were obtained with r^2 values greater than 0.995.

2.6. Transmission electron microscopy

The TEM images of the samples were obtained with a Philips CM 200 transmission electron microscope operating at 200 kV. All samples were dispersed in ethanol and deposited on the carbon-coated film prior to analysis.

2.7 Photocatalytic activity

Sulphorhodamine B, a fluorescent dye was obtained from Aldrich and diluted to $1.8 \times 10^{-5} \text{M}$ for use in the photocatalytic experiments.

The Ti-L samples, 0.075g, were dispersed in 150ml of $1.8 \times 10^{-5} \text{M}$ SRB and stirred for 30 mins in the dark to establish an equilibrium between adsorption and desorption of SRB on the catalyst. At this time, samples were collected and filtered through a Millipore filter to remove catalyst particles. The UV light source was a 100 W Hg lamp (NEC), with a wavelength of 254 nm. The stirred solutions were irradiated with UV light and further samples collected and filtered after 10, 20, 30, 45, 60, 75 and 90 mins of irradiation. The filtrates were examined on a UV-Vis spectrometer (Carey 100) to determine the concentration of SRB in the samples.

3. Results

3.1. X-Ray Diffraction

All XRD patterns exhibit the characteristic anatase diffraction peaks at 2θ values of: 25.3, 37.9, 47.6 and 54.8° [38]. The presence of brookite can also be confirmed by the appearance of its (121) peak at $2\theta = 30.8^\circ$. The anatase crystal sizes may be determined by measuring the line width at half maximum (B) of the anatase (101) peak at $2\theta = 25.3^\circ$ and employing this value in the Debye-Scherrer equation; $L = k\lambda/B \cos \theta$. Where L is the length of the crystal in the direction of the d spacing, k is a shape factor of the particle (1 if spherical, typically 0.9 is used), λ and θ are the wavelength and incident angle of the x-rays, respectively.

Typically, laponite exhibits a somewhat broad XRD pattern to indicate low crystallinity and small particle size [39]. Laponite diffraction peaks occur at 2θ values of approximately 5.6, 19.4, 27.5, 33.7 and 60.4 corresponding to (001), (100), (005), (110) and (300) crystal planes respectively [40].

3.1.1. HNO₃ Concentration

Figure 1 shows the XRD pattern of the TiO₂ sols prepared using 0.1M and concentrated HNO₃ as the peptising agent. The average diameter of the anatase particles prepared with both 0.1M and concentrated HNO₃ were determined using the Debye-Scherrer equation and found to be equivalent with sizes of approximately 6nm.

3.1.2. Hydrothermal Treatment of TiO₂

Figure 2 shows the XRD patterns of TiO₂ prepared with 0.1M HNO₃, without hydrothermal treatment, after microwave hydrothermal treatment and after hydrothermal treatment in an oven. Both patterns display characteristic anatase and brookite diffraction peaks. From these patterns, the anatase crystal sizes were determined to be approximately 4, 5 and 9nm respectively.

3.1.3. Synthesis pH

Figure 3 shows the XRD patterns of Ti-L samples prepared at pH values of 2, 6 and 9, labelled Ti-L-pH2, Ti-L-pH6, Ti-L-pH9 respectively. All patterns exhibit the diffraction peaks owing to anatase and brookite however, the laponite diffraction peaks are not as evident. These peaks are best seen for sample Ti-L-pH2, however the d001 peak has been replaced by a broad shoulder, indicating a reduction in the regularly ordered structure of the clay. Only minimal evidence of laponite peaks may be observed for samples Ti-L-pH6 and Ti-L-pH9, suggesting either a severe deterioration of clay order, or a lack of clay presence in the sample. The solution separated from the Ti-L-pH6 solid via centrifugation was rotary evaporated, and a white solid obtained, sample TiL-pH6-R, which when analysed via XRD was found to be laponite, shown in Figure 4, due to the presence of the d001 and d005 peaks. The average anatase crystal sizes of three samples were found to be approximately 5nm in diameter, as determined by the Debye-Scherrer equation.

3.1.4. Ti/ClayRatio

Using a polyethylene oxide surfactant, samples were prepared at a pH of <6, with Ti/clay ratios of 10, 20, 30 and 40mmol Ti/gram of clay. Figure 5 shows the XRD pattern of these samples, in which it is possible to see peaks attributed to anatase, brookite and laponite. An increase in the size of the anatase d101 peak can be observed as the concentration of Ti increases, whilst the clay peaks tend to decrease in size as Ti concentration increases. The anatase crystal sizes of the four samples are between 7-8nm, as determined by the Debye-Scherrer equation.

3.1.5 Hydrothermal Treatment of TiO₂-Laponite

An investigation of the effect of hydrothermal treatment of the combined TiO₂-laponite system was performed using the sample prepared with 40mmol Ti/gram laponite. One sample did not receive any hydrothermal treatment whilst the remaining were treated at temperatures of 80, 140 and 180°C. Figure 6 shows the XRD pattern of these samples. From this pattern, it can be determined using the Debye-Scherrer equation, that as the hydrothermal temperature increases, the anatase particle size increases marginally, from 5.5nm for Ti-L40-noHT to 7nm for Ti-L40-180.

3.2. Mid-IR Spectroscopy

Figure 7a and 7b show the infrared spectra of laponite. The high wavelength region of the spectrum is dominated by various stretching vibrations of the hydroxyl groups bonded to metallic cations and to water molecules. Bending of water molecules produces a peak close to 1630cm⁻¹ whilst the bonds characteristic of the tetrahedral layer of the clay dominate the region of low wavenumbers. The band at approximately 1000cm⁻¹ is assigned to the Si-O-Si bonds and is the most intense of the spectrum. The bands due to Metal-O bonds in the octahedral layer appear at low wavenumbers. These would be related predominantly to Mg-O and Li-O due to the chemical nature of laponite.

Figure 8 shows the infrared spectra of Ti-LpH2, Ti-LpH6 and Ti-LpH9. The band at 976cm^{-1} is present in the spectra of Ti-L-pH2 and Ti-L-pH6 can be attributed to the Ti-O-Si bond [41]. This peak is relatively small in the Ti-L-pH6 spectra and absent from Ti-L-pH9. Whilst the lower wavenumber region of Ti-LpH2 is very similar to that of laponite, the other two samples exhibit large broad bands in the region of $750\text{-}530\text{cm}^{-1}$, which can be attributed to the presence of discrete anatase particles in the samples [42].

3.4. Transmission Electron Microscopy

Figure 9 shows the TEM images of samples Ti-L-pH2, Ti-L-pH3, Ti-L-pH4 and Ti-L-pH5. The two distinct materials are present in the images; clay sheets and titania nanoparticles. At lower pHs the finite clay sheet structure is less readily observed, which could indicate a degree of metal leaching. Alternative tests would need to be performed to confirm this. Each sample shows some evidence of the dispersion of TiO_2 crystals on clay surfaces, however, the samples are not homogenous, with other regions containing larger agglomerates.

3.7 Photocatalytic Activity

Figure 10 shows the results of the photocatalytic tests of samples with varying Ti/clay ratios. It was found that as the concentration of Ti increased, the photocatalytic activity of the sample also increased. Ti-L40-180 exhibited a greater photo activity than samples Ti-L30-180, Ti-L20-180 and Ti-L10-180.

Figure 11 shows the photocatalytic results of samples treated at different hydrothermal temperatures. It was found that as the hydrothermal temperature increased, so did the photocatalytic activity of the sample. Ti-L40-180 exhibited higher photo activity than samples Ti-L40-140 and Ti-L40-80.

4. Discussion

4.1 HNO₃ Concentration

The crystal sizes of TiO₂ nanoparticles prepared with both 0.1M and concentrated HNO₃ as peptising agents are very similar, indicating that the acid concentration has a minimal effect on crystallite size in this synthesis.

4.2 Hydrothermal Treatment

Hydrothermal processing of inorganic materials, such as the high pressure convection heat treatment of a colloidal suspension, has a distinct effect on crystallite size and phase. Under these conditions, Ostwald ripening occurs, in which smaller particles dissolve in favour of the growth of larger crystals, resulting in an improved degree of crystallinity of the particles. Microwave hydrothermal treatment operates not by convection, but by a different mechanism, in which localised superheating occurs inducing rapid rates of crystallisation, whilst the bulk solution remains at a moderate temperature[37]. It has been shown to produce crystalline TiO₂ nanocrystals with a narrow size distribution in the range of 4-5nm [43].

The hydrothermal treatment method used in this experiment, appears to have a marked impact on the size of the anatase crystals, with those prepared in the microwave displaying average diameters of 5nm, 4nm less than those prepared in the oven. Hydrothermal treatment is a key parameter which can be altered to tailor crystal sizes.

4.2 Synthesis pH

The pH of the combined clay and TiO₂ systems is an important parameter in the synthesis. At high pH, (above 9), laponite exists as discrete exfoliated clay plates. However as the pH reduces, positive charges form on the rim of the clay plates leading to aggregation of the clay species in what is described as house-of-cards structure, as the positive rims are attracted to the negative clay faces. Tawari et al. suggest that at a pH of 11.7 the rim charge is neutralised [44, 45], thus edge-to-face aggregation is expected below this pH; increasing as the pH decreases. Additionally, TiO₂ colloids are stable at low pH (below 5.9, the isoelectric point for TiO₂), where the electrostatic repulsion occurring between positively charged TiO₂ particles is greater than the forces of van der Waals attraction occurring in the system. In order to find a suitable pH in which neither the clay nor the TiO₂ would experience significant aggregation, a range of synthesis pHs were examined.

From figures 3 and 4, it can be determined that at mid to high pHs, the majority of the TiO₂ does not adhere to the laponite, with the clay remaining exfoliated to such an extent that it will not settle via centrifugation. At pH values above the isoelectric point of TiO₂, the charge that appears on the TiO₂ particles is negative, hence explaining its lack of attraction to the negative clay faces.

The IR spectra in Figure 8b, provides further evidence of the lack of Ti-O-Si bonding in Ti-LpH9 and suggests a small amount of bonding of TiO₂ to clay in sample Ti-LpH6. It could be possible that the negatively charged TiO₂ particles have bonded to the positively charged rims of the clay plates in sample Ti-LpH6.

The anatase crystal size is not affected by the synthesis pH of the Ti-Lap mixture, however, pH can have an affect on particle size, due to increased aggregation of the TiO₂ at pH values near and above the isoelectric point of TiO₂. There is also a possibility, that in acidic conditions, the clay sheets can be damaged due to acid leaching.

Using a surfactant is one way of marrying the clay and TiO₂ systems, such that at a pH range of 2-6 agglomeration of the clay will be minimal, as the surfactant wraps around the clay particles, preventing the attraction between the positive clay rims and negative faces.

4.2 Ti/Clay Ratio

The TiO₂/clay ratio was found to have only a very minimal impact on crystallite size, with sizes ranging from 7-8nm for samples Ti-L10-180 to Ti-L40-180.

The TiO₂/clay ratio was found to have a significant effect on the photocatalytic activity of the sample. Ti-L40-180 exhibited a greater photoactivity than samples Ti-L30-180, Ti-L20-180 and Ti-L10-180, due to the greater amount of anatase active sites.

4.2 Hydrothermal Treatment of Ti-Laponite

Increasing the hydrothermal treatment temperature results in a slight increase in crystal size, 5.5nm for Ti-L40-noHT to 7nm for Ti-L40-180.

The photocatalytic activity increased significantly as the hydrothermal temperature increased, with Ti-L40-180 exhibiting higher photoactivity than samples Ti-L40-140 and Ti-L40-80. This is likely due to an increase in anatase crystallinity at greater hydrothermal temperatures.

5. Conclusions

Laponite-supported TiO₂ photocatalysts were produced and a variety of synthesis parameters examined in this study. The photocatalytic activity of the samples was improved by increasing the Ti/clay ratio to provide a greater number of active anatase sites, and also by the use of hydrothermal treatment which enhanced the anatase crystallinity.

Additional tests to characterise porosity and elemental composition are desired to further understand the properties of these materials, and determine their most suitable application.

Acknowledgments

The financial and infra-structure support of the Queensland University of Technology, Inorganic Materials Research Program is gratefully acknowledged. The Australian Research Council (ARC) is thanked for funding the instrumentation.

References

- [1] Z. Ding, H.Y. Zhu, G.Q. Lu, P.F. Greenfield, *Journal of Colloid and Interface Science* 209 (1999) 193-199.
- [2] J. Li, C. Chen, J. Zhao, H. Zhu, J. Orthman, *Applied Catalysis B: Environmental* 37 (2002) 331-338.
- [3] H.Y. Zhu, J.Y. Li, J.C. Zhao, G.J. Churchman, *Applied Clay Science* 28 (2005) 79-88.
- [4] Z. Ding, H.Y. Zhu, G.Q. Lu, P.F. Greenfield, *Encyclopaedia of Surface and Colloid Science* (2002) 4030-4042.
- [5] H. Zhu, X. Gao, Y. Lan, D. Song, Y. Xi, J. Zhao, *Journal of the Americal Chemical Society* 126 (2004) 8380-8381.
- [6] H.Y. Zhu, G.Q. Lu, *Materials Research Society Symposium Proceedings* 703 (2002) 9-18.
- [7] H.Y. Zhu, Y. Lan, X.P. Gao, S.P. Ringer, Z.F. Zheng, D.Y. Song, J.C. Zhao, *Journal of the Americal Chemical Society* 127 (2005) 6730-6736.
- [8] X. Duan, D. Sun, Z. Zhu, X. Chen, P. Shi, *Journal of Environmental Science and Health, Part A: Toxic/Hazardous Substances & Environmental Engineering* A37 (2002) 679-692.
- [9] H. Choi, E. Stathatos, D.D. Dionysiou, *Applied Catalysis B: Environmental* 63 (2005) 60-67.
- [10] G. Dobrescu, M. Crisan, M. Zaharescu, N.I. Ionescu, *Materials Chemistry and Physics* 87 (2004) 184-189.

- [11] A. Burns, G. Hayes, W. Li, J. Hirvonen, J.D. Demaree, S.I. Shah, *Materials Science and Engineering B* 111 (2004) 150-155.
- [12] I.N. Martyanov, K.J. Klabunde, *Journal of Catalysis* 225 (2004) 408-416.
- [13] J.A. Wang, A. Cuan, J. Salmenes, N. Nava, S. Castillo, M. Moran-Pineda, F. Rojas, *Applied Surface Science* 230 (2004) 94-105.
- [14] N.-L. Wu, M.-S. Lee, Z.-J. Pon, J.-Z. Hsu, *Journal of Photochemistry and Photobiology, A: Chemistry* 163 (2004) 277-280.
- [15] C. Wang, Q. Li, R.-D. Wang, *Materials Letters* 58 (2004) 1424-1426.
- [16] X. Li, X. Quan, C. Kotal, *Scripta Materialia* 50 (2004) 499-505.
- [17] K.L. Yeung, S.T. Yau, A.J. Maira, J.M. Coronado, J. Soria, P.L. Yue, *Journal of Catalysis* 219 (2003) 107-116.
- [18] R.M. Almeida, A.S. Rodrigues, *Journal of Non-Crystalline Solids* 326&327 (2003) 405-409.
- [19] H.E. Chao, Y.U. Yun, H.U. Xingfang, A. Larbot, *Journal of the European Ceramic Society* 23 (2003) 1457-1464.
- [20] W. Wang, M. Gu, Y. Jin, *Materials Letters* 57 (2003) 3276-3281.
- [21] B. Guo, Z. Liu, L. Hong, H. Jiang, J.Y. Lee, *Thin Solid Films* 479 (2005) 310-315.
- [22] P. Falaras, A.P. Xagas, *Journal of Materials Science* 37 (2002) 3855-3860.
- [23] M. Keshmiri, M. Mohseni, T. Troczynski, *Applied Catalysis B: Environmental* 53 (2004) 209-219.
- [24] K. Kordas, A.E. Pap, S. Leppavuori, *Surface and Coatings Technology* 176 (2003) 84-87.
- [25] C. Su, B.Y. Hong, C.M. Tseng, *Catalysis Today* 96 (2004) 119-126.

- [26] G. Dagan, S. Sampath, O. Lev, *Chemistry of Materials* 7 (1995) 446-453.
- [27] C.H. Kwon, J.H. Kim, I.S. Jung, H. Shin, K.H. Yoon, *Ceramics International* 29 (2003) 851-856.
- [28] N. Phonthammachai, T. Chairassameewong, E. Gulari, A.M. Jamieson, S. Wongkasemjit, *Microporous and Mesoporous Materials* 66 (2003) 261-271.
- [29] K.M.S. Khalil, A.A. Elsamahy, M.S. Elanany, *Journal of Colloid and Interface Science* 249 (2002) 359-365.
- [30] K. Guan, *Surface and Coatings Technology* 191 (2005) 155-160.
- [31] W. Que, Z. Sun, Y. Zhou, Y.L. Lam, Y.C. Chan, C.H. Kam, *Thin Solid Films* 359 (2000) 177-183.
- [32] Z. Jiwei, Y. Tao, Z. Liangying, Y. Xi, *Ceramics International* 25 (1999) 667-670.
- [33] W.-C. Huang, Method of producing quantum-dot powder and film via templating by a two-dimensional ordered array of air bubbles in a polymer. (USA). Application: US
US, 2003, p. 12 pp.
- [34] J.L. Valverde, P. Sanchez, F. Dorado, C.B. Molina, A. Romero, *Microporous and Mesoporous Materials* 54 (2002) 155-165.
- [35] M.N. Timofeeva, S.T. Khankhasaeva, S.V. Badmaeva, A.L. Chuvilin, E.B. Burgina, A.B. Ayupov, V.N. Panchenko, A.V. Kulikova, *Applied Catalysis, B: Environmental* 59 (2005) 243-248.
- [36] Y. Chen, K. Wang, L. Lou, *Journal of Photochemistry and Photobiology, A: Chemistry* 163 (2004) 281-287.

- [37] S.-Z. Chu, K. Wada, S. Inoue, S. Todoroki, *Chemistry of Materials* 14 (2002) 266-272.
- [38] W. Li, M. Sirilumpen, R.T. Yang, *Applied Catalysis, B: Environmental* 11 (1997) 347-363.
- [39] H.J.M. Hanley, C.D. Muzny, B.D. Butler, *Langmuir* 13 (1997) 5276-5282.
- [40] S.L. Tawari, D.L. Koch, C. C., *Journal of Colloid and Interface Science* 240 (2001) 54-66.
- [41] H.A. Baghdadi, H. Sardinha, S.R. Bhatia, *Journal of Polymer Science, Part B: Polymer Physics* 43 (2004) 233-240.
- [42] G.J. Wilson, A.S. Matijasevich, D.R.G. Mitchell, J.C. Schulz, G.D. Will, *Langmuir* 22 (2006) 2016-2027.
- [43] H.Y. Zhu, J.A. Orthman, J.-Y. Li, J.-C. Zhao, G.J. Churchman, E.F. Vansant, *Chemistry of Materials* 15 (2002) 5037-5044.
- [44] M. Park, I.-K. Shim, E.-Y. Jung, J.-H. Choy, *Journal of Physics and Chemistry of Solids* 65 (2004) 499-501.
- [45] P.X.P. Highscore.
- [46] H.Y. Zhu, Ding, Z. and Barry, J.C., *Journal of Physical Chemistry* 106 (2002) 11420-11429.
- [47] H.W.a.B. Van Der Marel, H., *Atlas of Infrared Spectroscopy of Clay Minerals and their Admixtures*, Elsevier Scientific Publishing Company, Oxford, 1976.
- [48] G.J. Wilson, Will, Geoffrey D., Frost, Ray L. and Montgomery, Simon A., *Journal of Materials Chemistry* 12 (2002) 1787-1791.

List of Figures

Figure 1 XRD patterns of TiO₂ (a) prepared with 0.1M and (b) concentrated HNO₃ as a peptising agent.

Figure 2 XRD patterns of TiO₂ (a) colloid, (b) colloid after microwave hydrothermal treatment, and (c) colloid after oven hydrothermal treatment.

Figure 3 XRD patterns (a) Ti-LpH2, (b) Ti-LpH6 and (c) Ti-LpH9.

Figure 4 XRD patterns of Ti-LpH6 obtained via (a) centrifugation (Ti-LpH6-C) and (b) rotary evaporation (Ti-LpH6-R).

Figure 5 XRD patterns of (a) Ti-L10-180, (b) Ti-L20-180, (c) Ti-L30-180 and (d) Ti-L40-180.

Figure 6 XRD patterns of (a) Ti-L40-no-HT, (b) Ti-L40-80, (c) Ti-L40-140 and (d) Ti-L40-180.

Figure 7a Infrared spectra of laponite in the 2500-4000cm⁻¹ region.

Figure 7b Infrared spectra of laponite in the 550-1800cm⁻¹ region.

Figure 8 Infrared spectra of samples Ti-LpH2, Ti-LpH6, Ti-LpH9 in the 550-1800cm⁻¹ region.

Figure 9 TEM images of (a) Ti-LpH2, (b) Ti-LpH3 (c) Ti-LpH4 (d) Ti-LpH5

Figure 10 Graph of photocatalytic activity of Ti-L10-180, Ti-L20-180, Ti-L30-180 and Ti-L40-180.

Figure 11 Graph of photocatalytic activity of Ti-L40-180, Ti-L40-140 and Ti-L40-80.

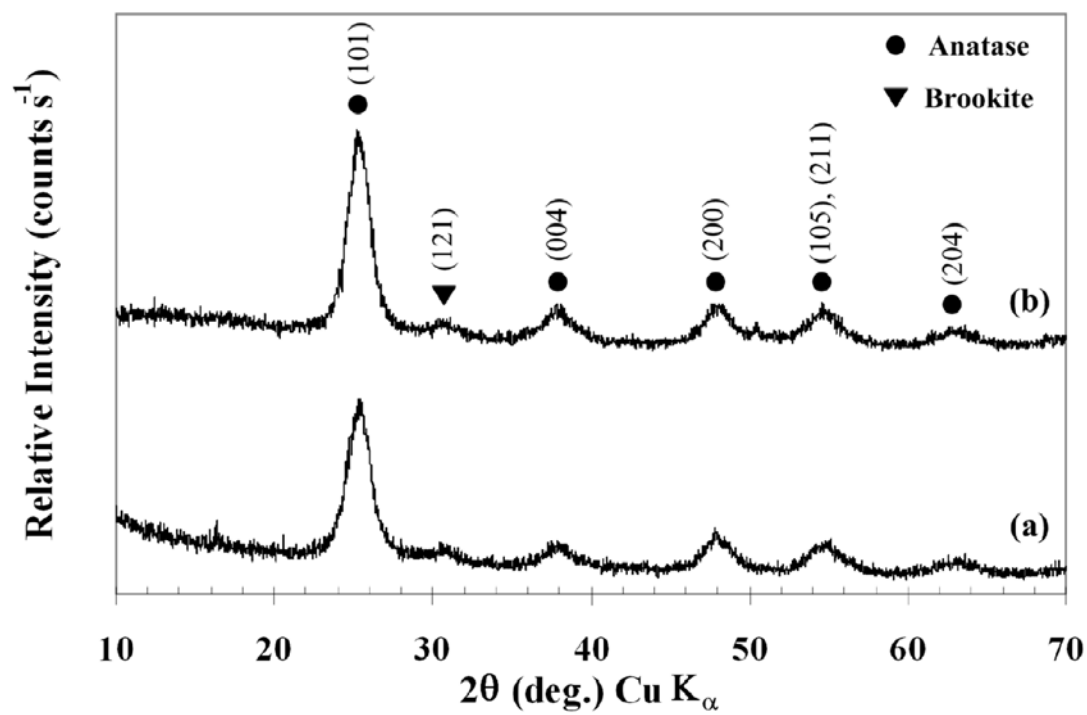


Figure 1

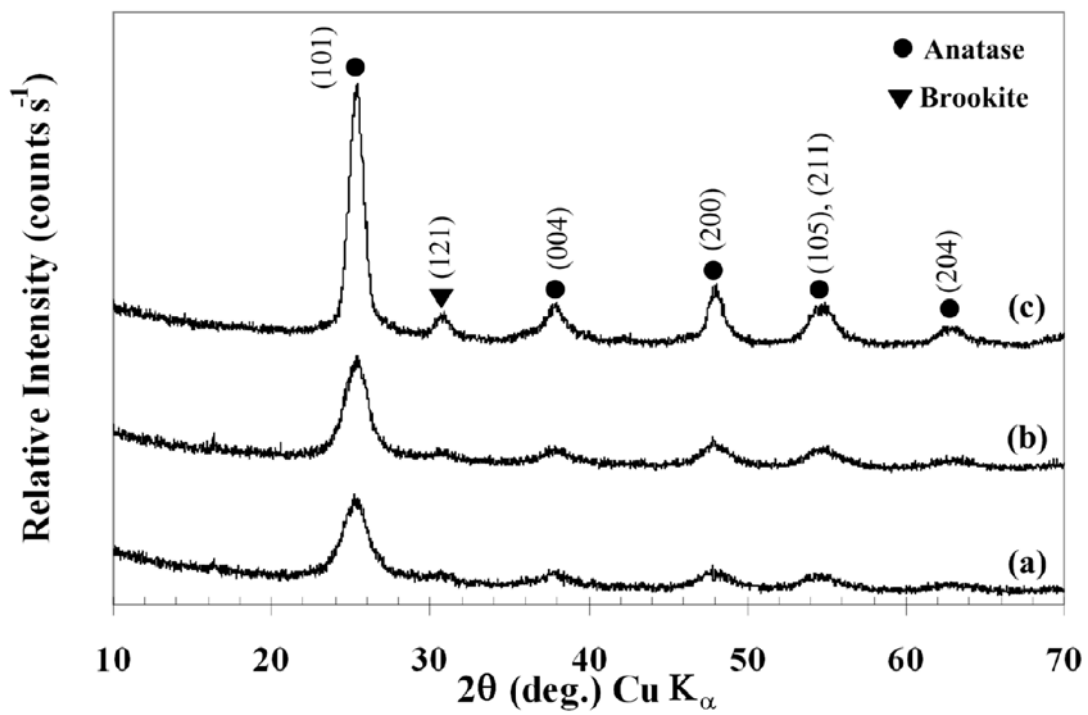


Figure 2

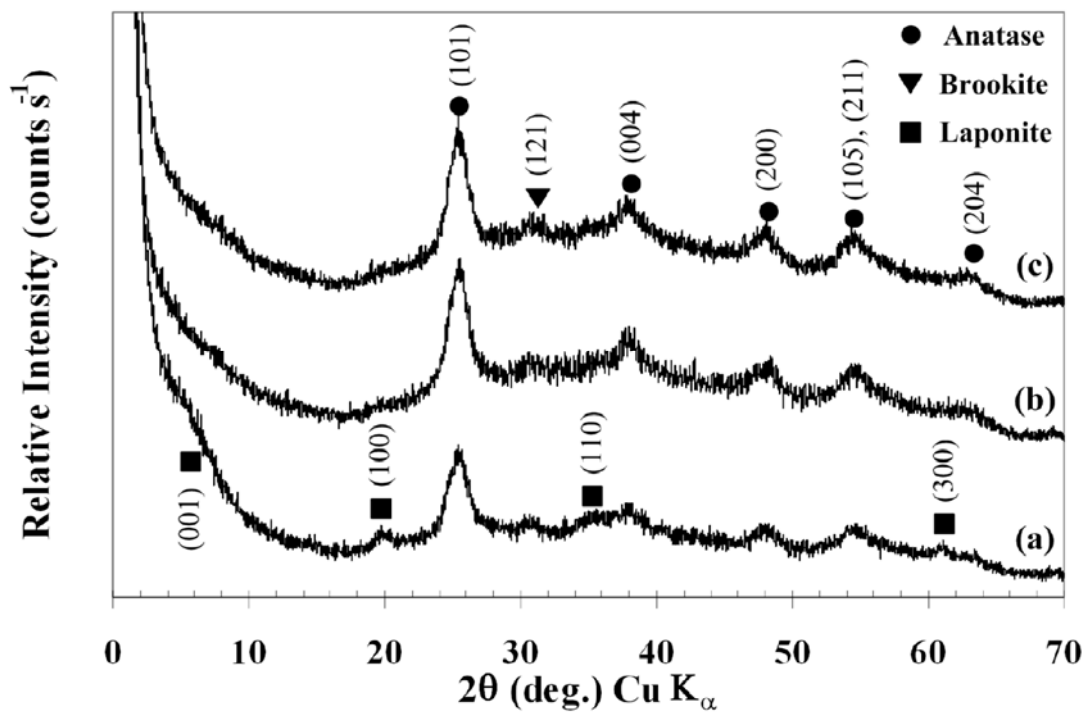


Figure 3

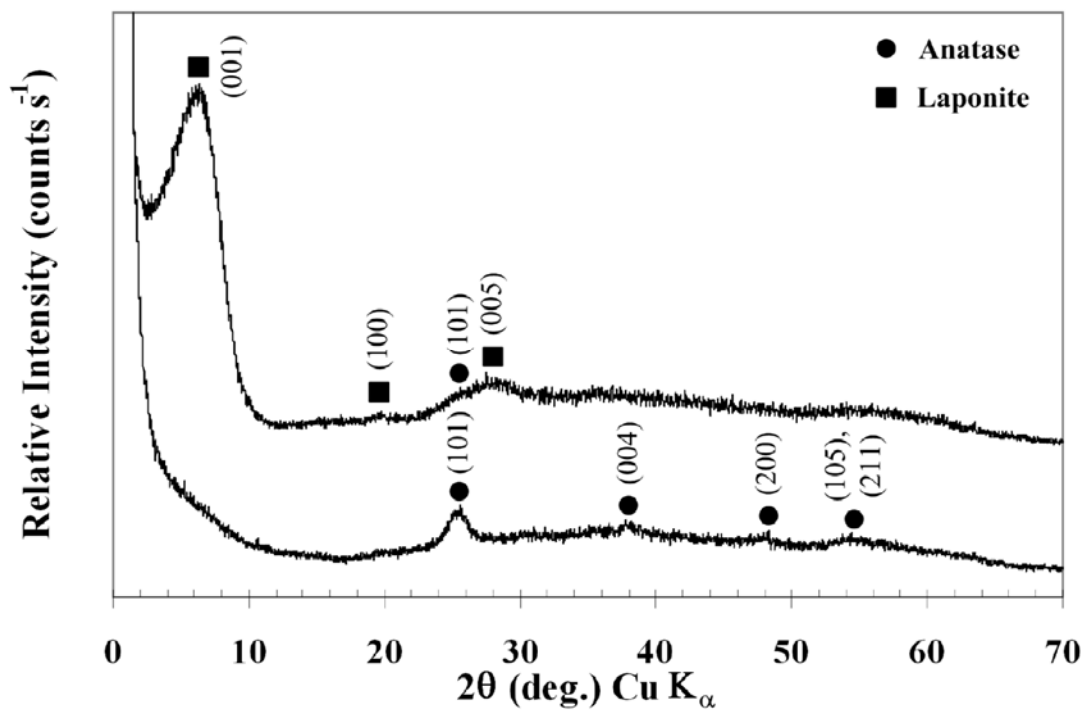


Figure 4

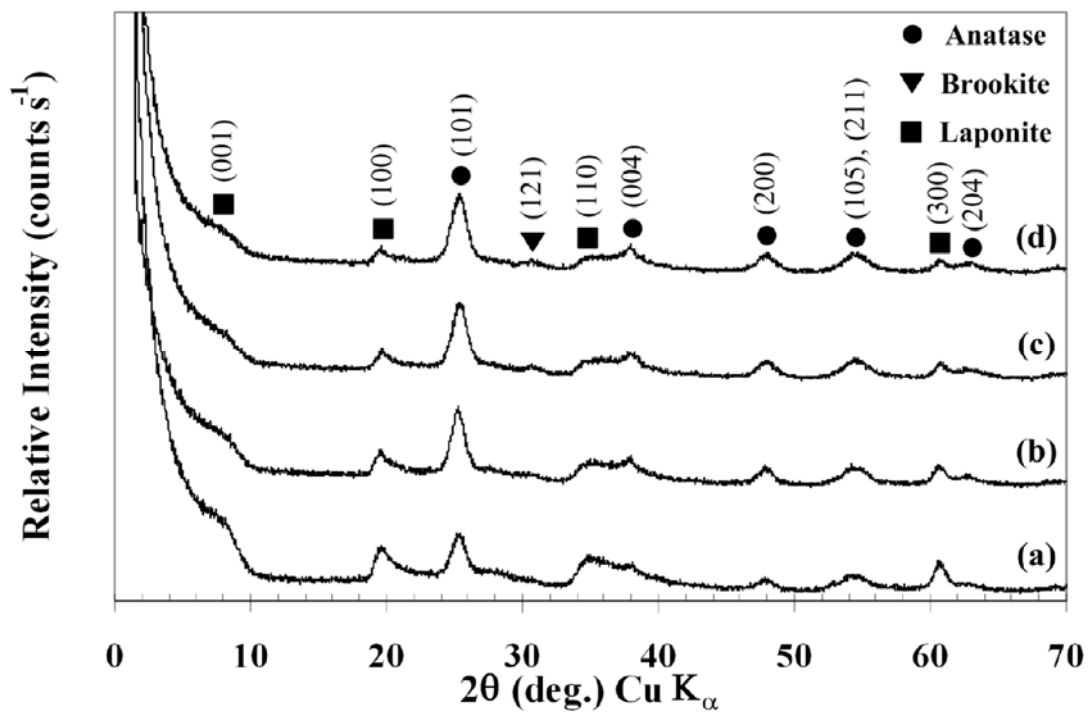


Figure 5

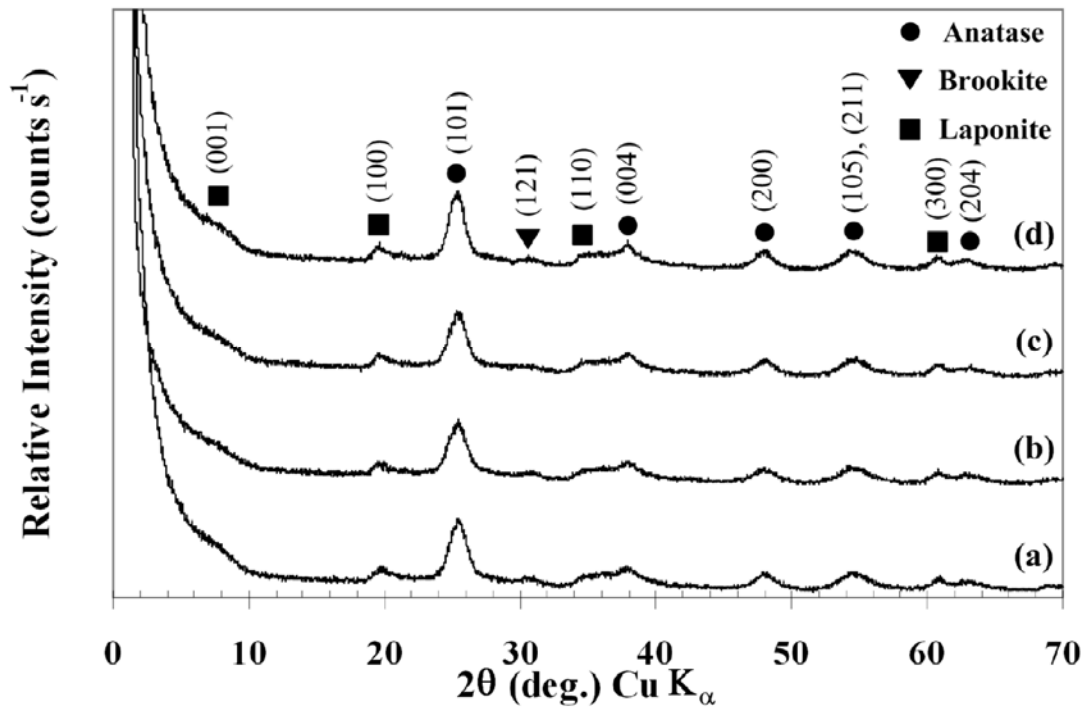


Figure 6

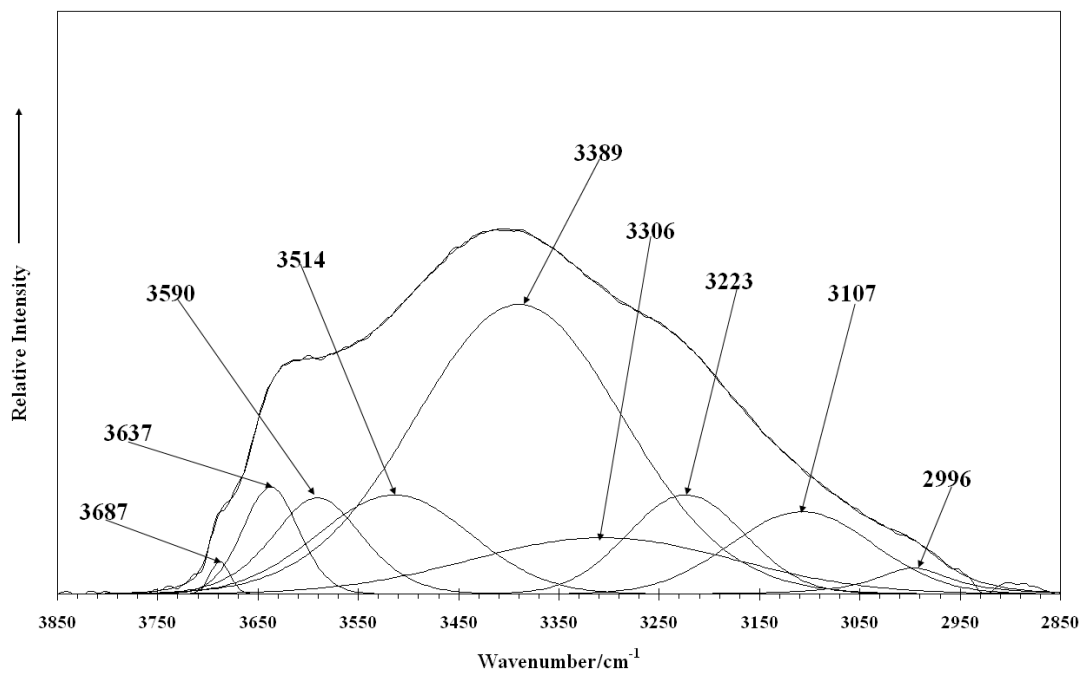


Figure 7a

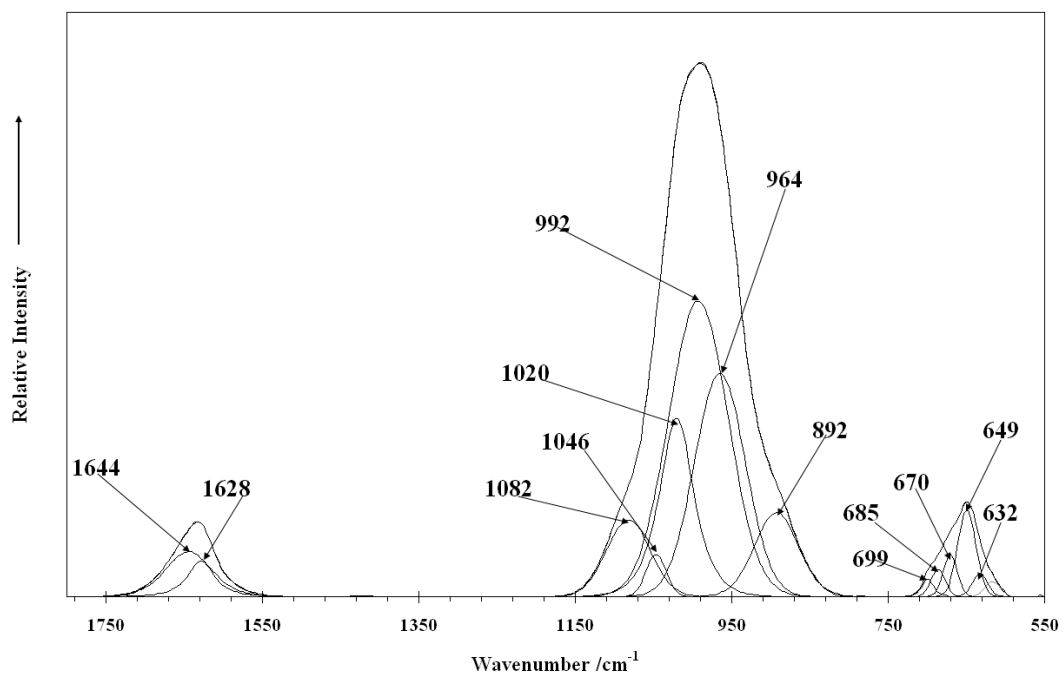


Figure 7b

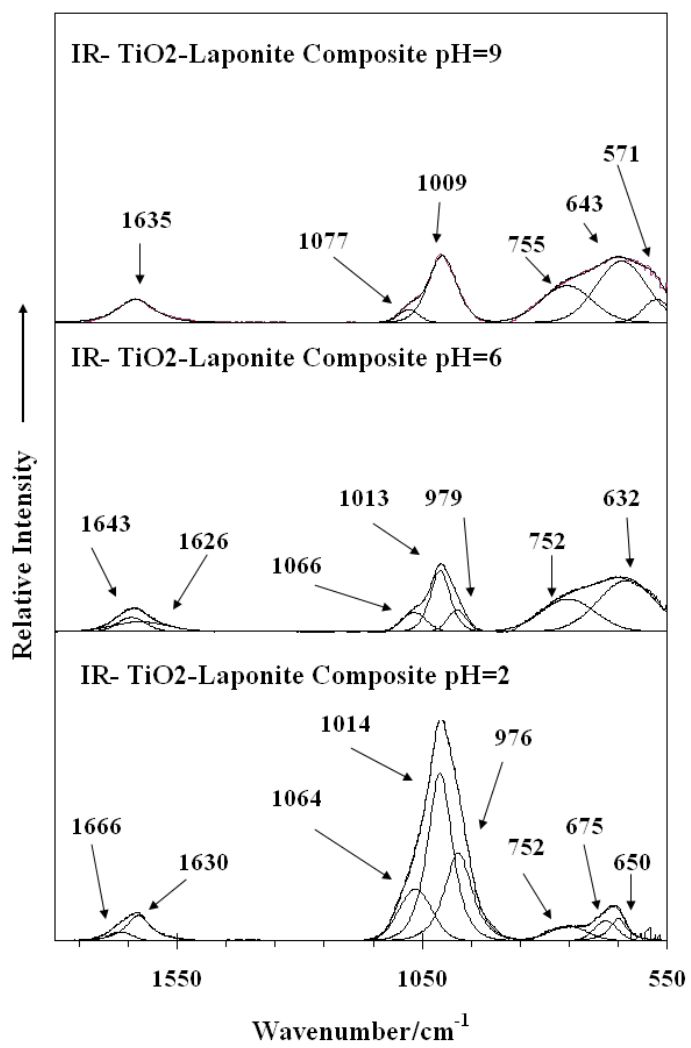


Figure 8

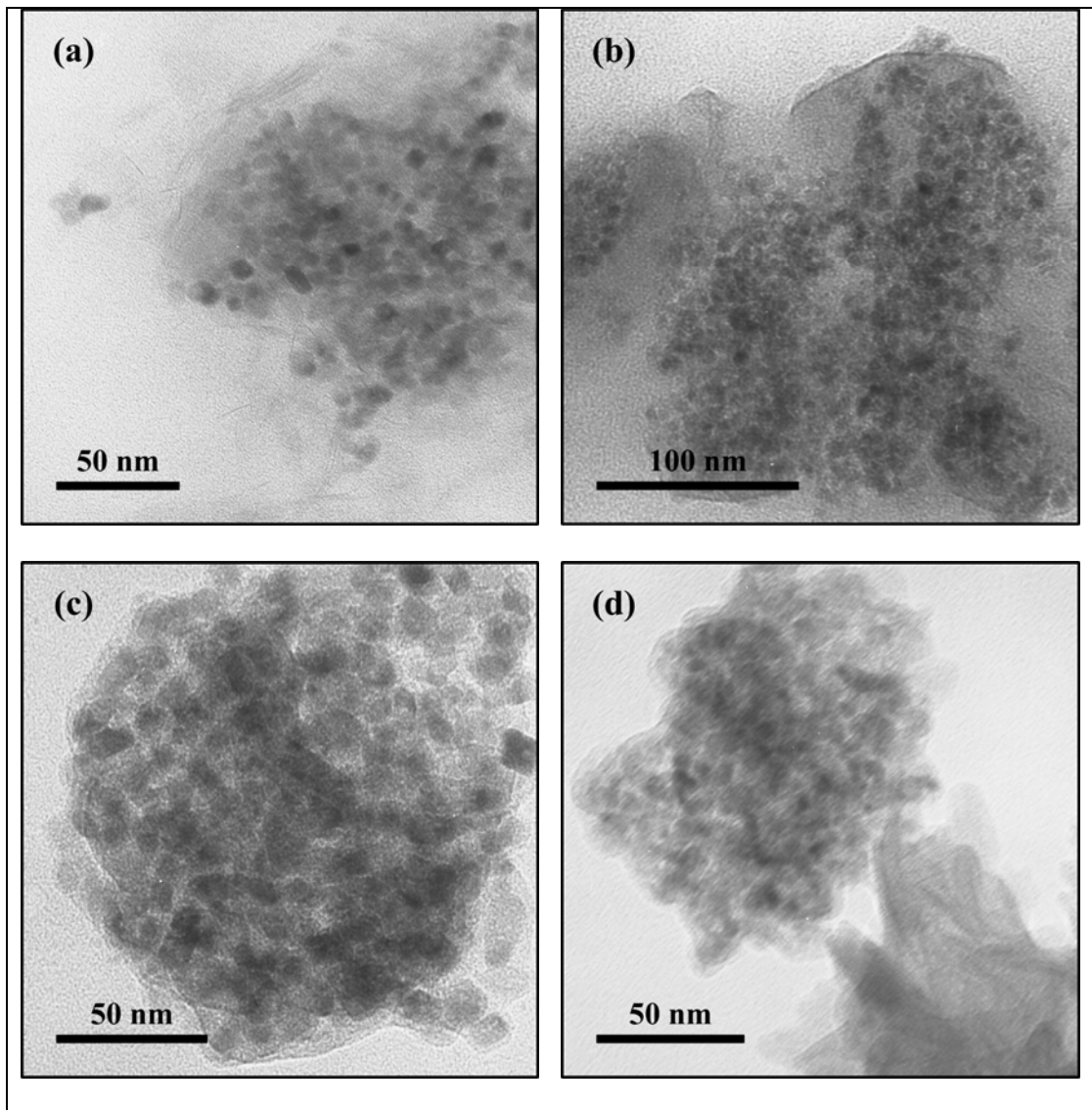


Figure 9

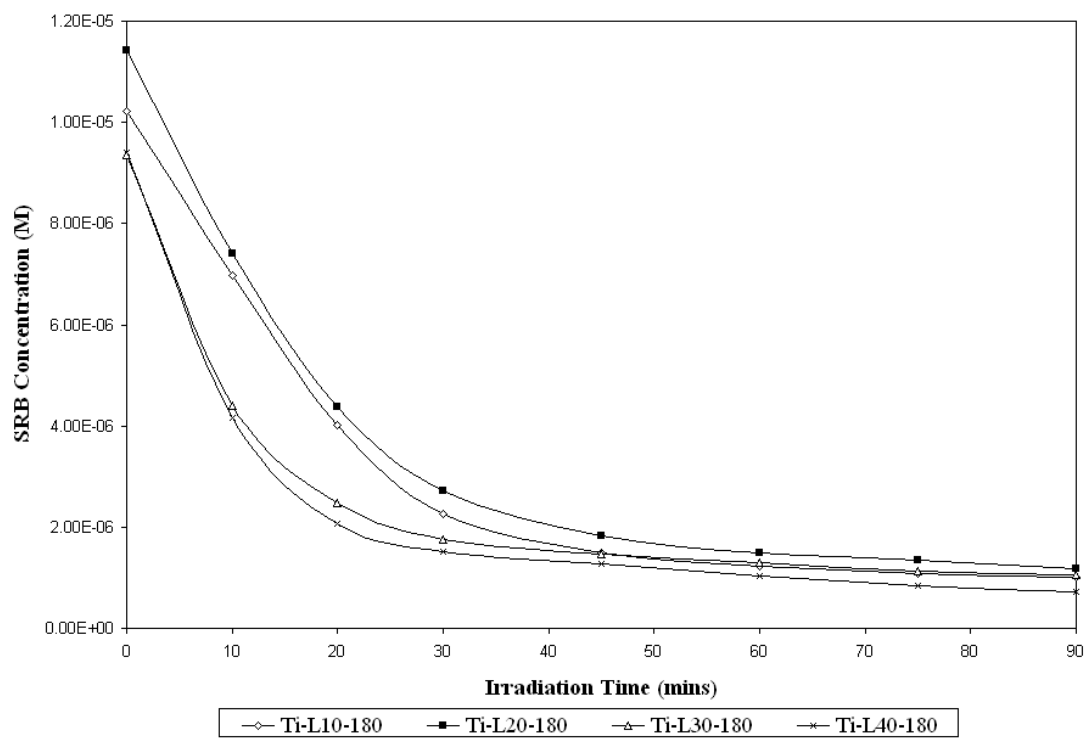


Figure 10

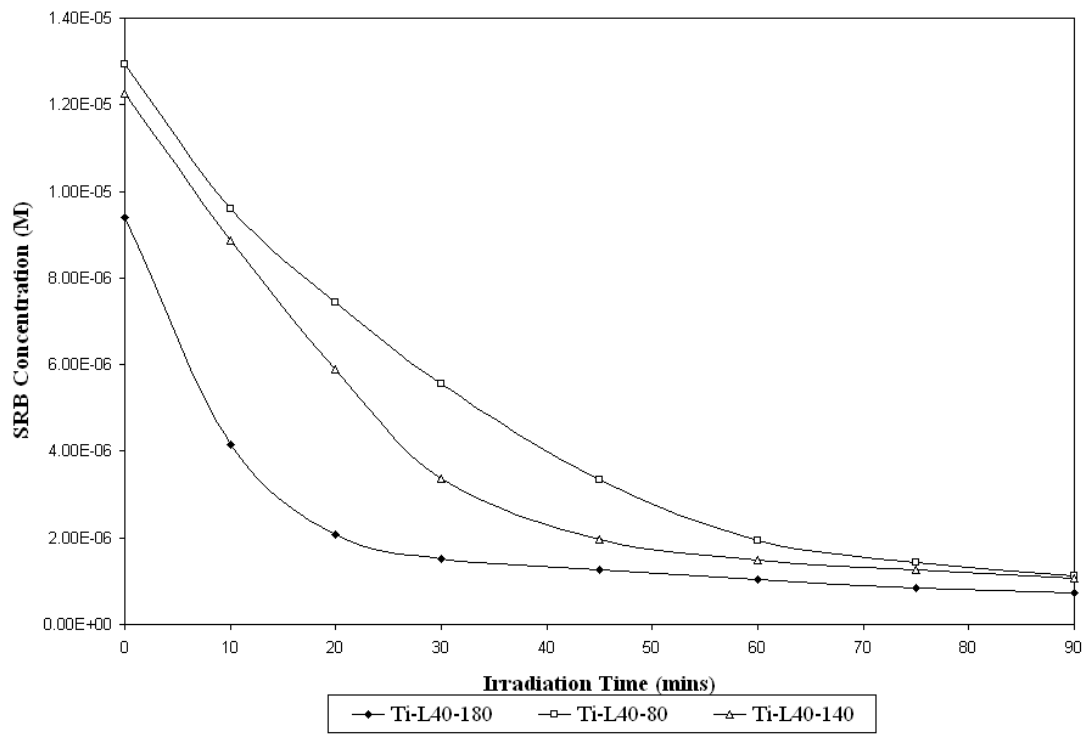


Figure 11